Journal of Biomedical Optics

BiomedicalOptics.SPIEDigitalLibrary.org

Hybrid piezoresistive-optical tactile sensor for simultaneous measurement of tissue stiffness and detection of tissue discontinuity in robot-assisted minimally invasive surgery

Naghmeh M. Bandari
Roozbeh Ahmadi
Amir Hooshiar
Javad Dargahi
Muthukumaran Packirisamy

SPIE.

Naghmeh M. Bandari, Roozbeh Ahmadi, Amir Hooshiar, Javad Dargahi, Muthukumaran Packirisamy, "Hybrid piezoresistive-optical tactile sensor for simultaneous measurement of tissue stiffness and detection of tissue discontinuity in robot-assisted minimally invasive surgery," *J. Biomed. Opt.* **22**(7), 077002 (2017), doi: 10.1117/1.JBO.22.7.077002.

Hybrid piezoresistive-optical tactile sensor for simultaneous measurement of tissue stiffness and detection of tissue discontinuity in robot-assisted minimally invasive surgery

Naghmeh M. Bandari,[a,b] Roozbeh Ahmadi,[a,b] Amir Hooshiar,[b] Javad Dargahi,[b] and Muthukumaran Packirisamy[a,*]
[a]Concordia University, Optical-Bio Microsystems Laboratory, Mechanical and Industrial Engineering Department, Montreal, Canada
[b]Concordia University, Tactile Sensing and Medical Robotics Laboratory, Mechanical and Industrial Engineering Department, Montreal, Canada

Abstract. To compensate for the lack of touch during minimally invasive and robotic surgeries, tactile sensors are integrated with surgical instruments. Surgical tools with tactile sensors have been used mainly for distinguishing among different tissues and detecting malignant tissues or tumors. Studies have revealed that malignant tissue is most likely stiffer than normal. This would lead to the formation of a sharp discontinuity in tissue mechanical properties. A hybrid piezoresistive-optical-fiber sensor is proposed. This sensor is investigated for its capabilities in tissue distinction and detection of a sharp discontinuity. The dynamic interaction of the sensor and tissue is studied using finite element method. The tissue is modeled as a two-term Mooney–Rivlin hyperelastic material. For experimental verification, the sensor was microfabricated and tested under the same conditions as of the simulations. The simulation and experimental results are in a fair agreement. The sensor exhibits an acceptable linearity, repeatability, and sensitivity in characterizing the stiffness of different tissue phantoms. Also, it is capable of locating the position of a sharp discontinuity in the tissue. Due to the simplicity of its sensing principle, the proposed hybrid sensor could also be used for industrial applications. [DOI: 10.1117/1.JBO.22.7.077002]

Keywords: hybrid tactile sensor; piezoresistive; optical fiber; stiffness; tissue distinction; sharp discontinuity.

Paper 170082RR received Mar. 4, 2017; accepted for publication Jun. 26, 2017; published online Jul. 22, 2017.

1 Introduction

During the last decade, robot-assisted minimal invasive surgeries (RAMIS) have been introduced as an alternative to the surgeon-operated minimally invasive surgeries (MIS) to enhance the precision and dexterity of tool maneuvering. RAMIS could open a new horizon to health care providers seeking a reliable solution for remote surgeries. Despite the advantages of RAMIS to both surgeon and patient, losing the sense of touch is a major shortcoming.[1,2] The first generation of the da Vinci® surgical system (Intuitive Surgical, Inc., Sunnyvale, California), with >3400 units sold worldwide, did not provide surgeons with haptic feedback during tissue manipulation.[1] Surgeons usually palpate the tissues to have a perception of its stiffness to identify if it is a malignant mass, an artery, or a nerve. To compensate for the lack of haptic and tactile information, haptic feedback systems, using tactile sensors and actuators, were introduced as a part of RAMIS surgical units.[1,2] Furthermore, the haptic feedback systems prevented tissue laceration by limiting the holding force that surgeons were able to apply.[1,3–5] It has been experimentally shown that providing tactile feedback would lead to less grasping force in the da Vinci™ system.[6,7] In this regard, King et al.[6,7] integrated a FlexiForce™ force sensor on the surgical tool of the da Vinci™ system and transmitted the grasping force to the surgeons. Their study revealed that the force feedback could reduce the grasping forces during the operations significantly.[6,7] Also, other researchers have equipped surgical graspers with tactile sensors to assess the stiffness of the tissue.[8–11] Figure 1 shows a typical setup for robotic surgery in an operation room as well as a conceptual integration of a force sensor on a grasper of the da Vinci™ system.

Constitutively, most living tissues show a viscoelastic mechanical behavior.[12,13] A major phenomenon associated with the viscoelasticity of these tissues is the stress relaxation under sustained grasping pinch,[12] which results in an exponential depreciation in the contact force between the surgical tool and the tissue. Depending on the microstructure of tissue, the time constant of this stress relaxation can range anywhere between one-tenth of a second and several minutes.[13] This phenomenon leads to a dynamic interaction force between the surgical tool and tissue. The major limitations in developing a tactile sensor for minimally invasive surgical applications are size, biocompatibility, electro-passivity, magnetic resonance (MR) compatibility, and x-ray opacity.[14]

The tactile sensors proposed in the literature are designed based on electrical or optical sensing principles.[15] Electric tactile sensors mainly employ variable capacitance, piezoelectricity, and piezoresistivity phenomena, and[16] therefore, they are not MR-compatible and electro-passive. However, electric sensors possess simple sensing principles and are capable of direct force measurement. Also, electrical sensors are scalable to different

*Address all correspondence to: Muthukumaran Packirisamy, E-mail: mpackir@encs.concordia.ca

1083-3668/2017/$25.00 © 2017 SPIE

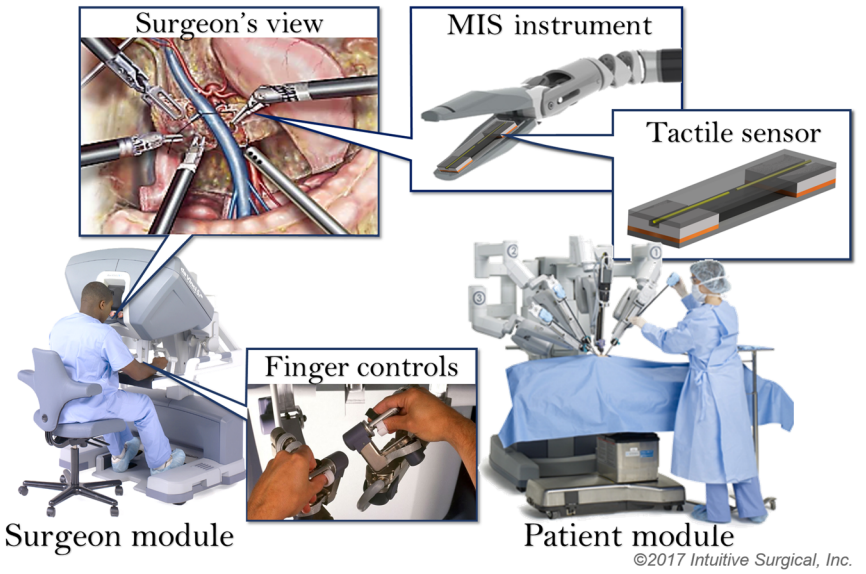

Fig. 1 Conceptual overview of a tactile sensor embedded in an MIS grasper. A surgeon uses the finger controls of the surgeon module to perform surgery. MIS instruments, equipped with tactile sensors, can help surgeons in tissue distinction. [Reproduced with permission, courtesy of (Intuitive Surgical Inc., California)].

length scales. These properties have led researchers to use such sensors in the minimally invasive surgical applications where MR compatibility and x-ray opacity are not a clinical priority,[17] for example, gastrointestinal surgeries.

On the other hand, optical-based sensors satisfy MR compatibility, electro-passivity, and size conditions; therefore, they make a good choice in minimally invasive surgical applications.[14,17–20] In addition to that, possibilities for miniaturization and low-cost production are of remarkable advantages of optical-based sensors;[21,22] however, optical-based sensors are not capable of direct force measurement. On the other hand, because of the nonlinear mechanical properties of the biological tissues, establishing a simple and valid force estimation scheme from the measured deformation is cumbersome.

Researchers have developed optical tactile sensors based on three sensing principles of fiber brag grating (FBG), Fabry–Perot interferometry (FPI), and light-intensity modulation (LIM).[21,22] In an early study, Polygerinos et al.[20] proposed a miniaturized optical fiber sensor for measuring the point loads at the tips of angiographic catheters; however, the proposed sensor was unable to measure the actual lateral forces acting on the tip of the catheter. In another study, Yip et al.[23] developed an LIM force sensor for surgical application based on the deformation-induced intensity modulation in a set of optical fibers.

Elayaperumal et al.[24] demonstrated a triaxial tip-force sensing needle to provide the real-time haptic feedback during surgery. In their study, an FBG sensor was attached to a biopsy needle for strain measurement. Recently, Qiu et al.[25] developed an FPI force sensor equipped with a miniaturized quantitative optical coherence elastography. Their sensor was capable of *in situ* estimation of the elastic modulus of a biological tissue based on the simultaneous measurement of force and deflection in it. Similarly, Noh et al.[26] proposed a miniaturized triaxial LIM force sensor, mounted at the tip of a cardiac ablation catheter to measure the contact force. In their study, the deflection-induced change in the light intensity carried by three optical fibers was measured using a CCD camera and a multilinear calibration scheme was used for force estimation.

In an early effort, researchers of this study developed an optical sensor working based on the bending intensity-modulation sensing principle. That sensor was capable of estimating the external force and locating a hidden mass inside a tissue phantom discretely in four regions.[27] However, it was neither miniaturized nor capable of estimating the stiffness of tissue. In continuation, highly sensitive sensors based on the intensity loss in a coupling gap were developed.[28–31] This could significantly improve the sensitivity of sensors and simplify the designs. Despite the improvements, accurate force estimation and hidden mass location were yet to be addressed.

To address the common problem of precise force measurement in RAMIS applications, a hybrid force sensor was designed, modeled, simulated, fabricated, and experimentally verified in this study. This hybrid sensor uses sensing principle of piezoresistivity, to directly measure the contact force and intensity modulation in optical fibers, also to estimate the deformation in the tissue (Fig. 2). The idea of hybrid sensing is to increase the accuracy of the sensor by replacing "force estimation" with "direct force measurement." In addition, piezoresistive sensors exhibit scalability, linearity, low hysteresis, and low noise. Also, such sensors can work under both static and dynamic conditions while maintaining acceptable repeatability.[32] By this design, the sensor is capable of estimating the stiffness of the tissue being contacted and can also measure the ratio of force in two separate piezoresistive sensing elements and detect the position of a hidden mass in tissue. Detecting stiffened tissues or masses is a routine exercise performed by surgeons through palpation in open surgeries.[33] Various studies have shown that it is very likely that malignant masses or tumors have a higher stiffness than the surrounding tissue.[34–36]

In the following sections, the geometrical design and sensing principles are introduced, finite element modeling is elaborated, and the microfabrication of the sensor and experimental setup is explained. Also, the results of the modeling and experimental

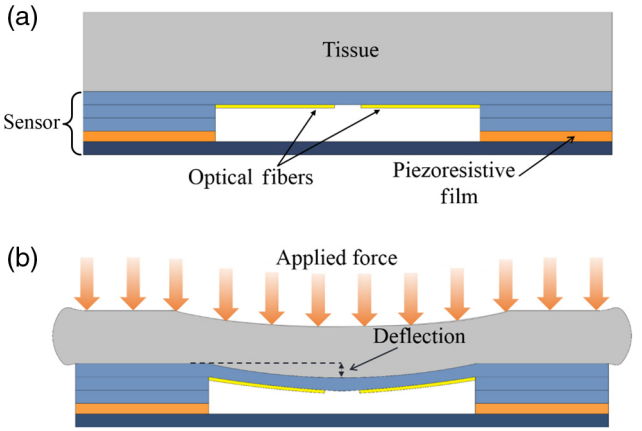

Fig. 2 Schematic of the tissue and sensor: (a) without contact load and (b) with contact load applied from the gripping surgical tool, which leads to a deflection in both the sensor and tissue.

parts are presented and discussed. Concluding remarks are the final part of this article.

2 Sensor Design and Sensing Concept

2.1 *Sensor Design*

A schematic of the three-dimensional (3-D) hybrid force sensor proposed in this study is shown in Fig. 3. The sensor incorporates two piezoresistive force sensing elements, two separate optical fibers, and eight silicon structural elements. A V-groove is bulk micromachined on the bottom surface of the beam on which two optical fibers were placed with a fixed gap [Fig. 3(a)]. The beam is fixed on the supports. The substrate, piezoelectric elements, and the chips form a sandwich configuration to transfer the interaction force from the beam to the substrate [Fig. 3(c)]. Each piezoresistive element consists of a piezoresistive film and two copper shell electrodes. One of the optical fibers was connected to a light source while the other was connected to a photodetector.

2.2 *Sensing Concept*

In the proposed sensor, the gap between the fibers resulted in a predictable initial coupling power loss. Additionally, the deflection of the beam developed an angular misalignment between two fibers. This misalignment would lead to further power loss between fibers (Fig. 4); therefore, the total loss of the power between fibers was due to both gap and angular misalignment.

The basic sensing concept behind this design was to measure the gap power loss by comparing the input power to the first fiber, P_i, with the output power of the second fiber, P_o. Nemoto and Makimoto[37] used geometrical optics principles and Gaussian distribution of the power spectrum on the cross section of an optical fiber to quantify the power loss due to coupling gap and misalignment between the two identical fibers. Gaussian distribution of the power spectrum is widely used by researchers as an acceptable approximation of the exact power spectrum distribution in optical fibers.[37–40] Li et al.[38] enhanced the study conducted by Nemoto et al. by considering the parabolic propagation of light into space and introduced the coupling efficiency, η, defined as the logarithmic measure of the input power with respect to the output power. Recently, Ahmadi et al.,[29] successfully applied the same method in prediction of the total power loss due to both gap and angular misalignment.

To determine the stiffness of the tissue, the maximum deformation resulting from the contact force was measured. This contact force is developed upon a sensor touching a tissue and causing a deflection in both tissue and sensor. As Fig. 2 shows, the maximum deformation in the tissue is equal to the maximum deflection of the beam u_{max}. In this sensor, the total contact force was measured by the piezoresistive sensing elements. To measure the maximum deflection, a theoretical framework was used as described below.

In Fig. 4, the distance between the fibers is represented by g, angular misalignment by $\Delta\theta$, total equivalent contact force by F_{eq}, and position of center of pressure by d_{eq}. In this framework, by using F_{eq} and d_{eq}, both distributed contact forces (large and flat tissues) and point contact forces (small and round tissues) are modeled. Because of the symmetry, the eccentricity and deflection of fibers in the y-direction was neglected [Fig. 3(d)]. As the output voltage of the photodetector is a linear function of the transmitted power between fibers,[29] the transmitted power (P_o) was obtained using the output voltage of the photodetector. The constant input power (P_i) was provided by a light source. Comparing output and input powers, the coupling efficiency (η) was calculated using Eq. (1), whereas Eq. (2) defines the coupling efficiency as a function of both axial gap and angular misalignment.[37,38] As the gap (g) was assumed to remain constant throughout the deformation (small deformation assumption), the

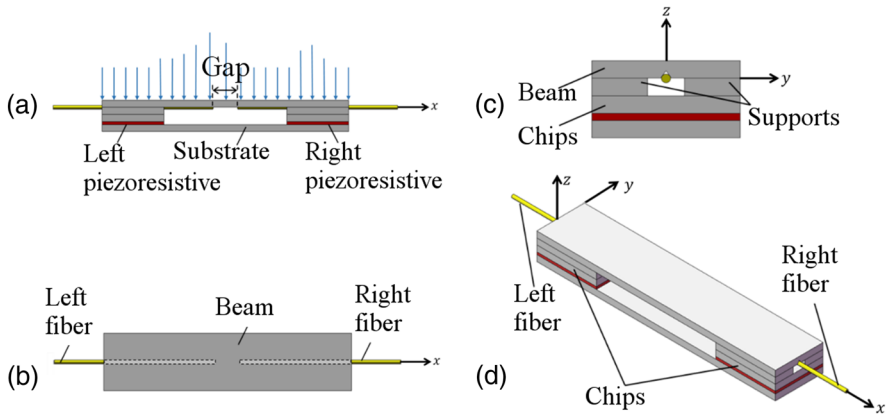

Fig. 3 The structural design of the hybrid sensor in (a) lateral, (b) top, (c) longitudinal, and (d) perspective view.

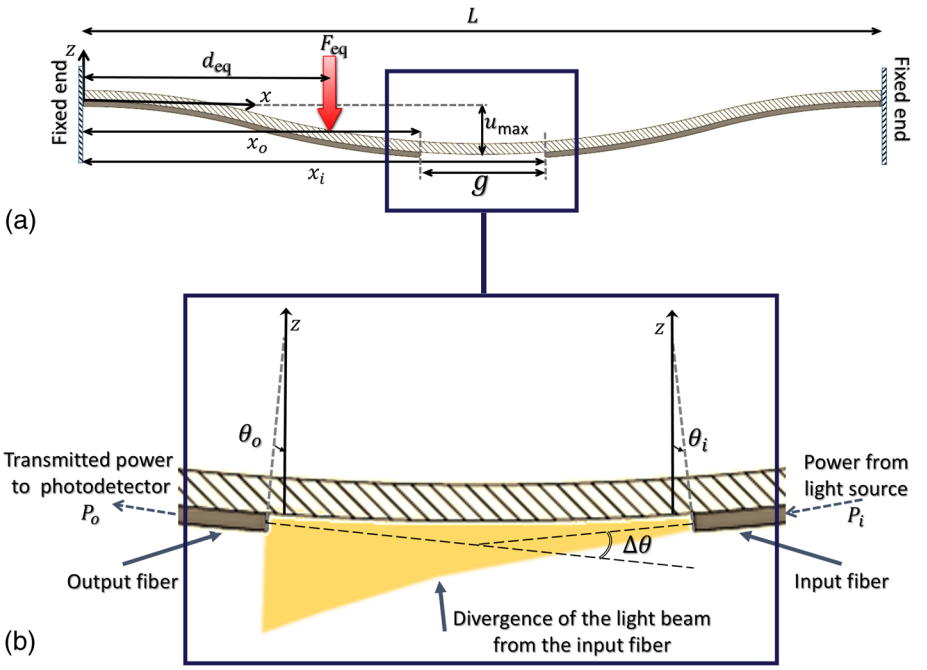

Fig. 4 (a) Schematic view of the deformed configuration of the sensor beam and optical fibers and (b) detailed view of the gap between two optical fibers and formation of the angular misalignment, $\Delta\theta = |\theta_i| + |\theta_o|$ as a result of vertical deformation in the beam and movement of the fiber tips.

coupling efficiency was merely a function of angular misalignment $\Delta\theta$. Therefore, Eq. (2) was solved for $\Delta\theta$ to estimate the angular misalignment from the coupling efficiency.

$$P_o = \eta P_i, \tag{1}$$

$$\eta = 4\frac{1}{B}e^{(-A\frac{C}{B})}, \tag{2}$$

where

$$A = 2\left(\frac{\pi w n_0}{\lambda}\right)^2, \tag{3}$$

$$B = 4 + \left(\frac{g\lambda}{\pi n_0 w^2}\right)^2, \tag{4}$$

$$C = \left[2 + \left(\frac{g\lambda}{\pi n_0 w^2}\right)^2\right]\sin^2(\Delta\theta), \tag{5}$$

in which λ is the wavelength of the light and n_0 is the refractive index of the air. The Gaussian mode field radius of optical fibers (w) was calculated using

$$W = a\left(0.65 + \frac{1.619}{H^{3/2}} + \frac{2.879}{H^6}\right), \tag{6}$$

where

$$H = \frac{2\pi a}{\lambda}\sqrt{n_1^2 - n_2^2}, \tag{7}$$

in which a, n_1, and n_2 were the radius of the core, refractive index of the core, and refractive index of the cladding of optical fibers, respectively.

To calculate the deflection indicated in Fig. 2, a composite beam problem consisted of both tissue materials, and a beam of the sensor was solved. Figure 4 represents a composite beam problem for finding the deflection of beam (u_z). The analytic solution for the displacement in this problem is provided in Eq. (8).[41] By taking derivation of displacement u_z with respect to length x, the angular deformation $\theta(x)$ was obtained [Eq. (9)]. Furthermore, the angular misalignment $\Delta\theta$ was calculated by summation of absolute angular deformations at the tip of both fibers [Eq. (10)].

$$u_z(x) = \begin{cases} \frac{F_{eq}(L-d_{eq})^2x^2}{6E_cI_cL^3}[3d_{eq}(L-x) - (L-d_{eq})x] & x < d_{eq} \\ \frac{F_{eq}(d_{eq})^2x^2}{6E_cI_cL^3}[3(L-d_{eq})(L-x) - (d_{eq})x] & x \geq d_{eq} \end{cases}, \tag{8}$$

$$\theta(x) = \frac{d}{dx}u_z(x) = \begin{cases} \frac{F_{eq}(L-d_{eq})^2x}{2E_cI_cL^3}[2d_{eq}(L-x) - Lx] & x < d_{eq} \\ \frac{F_{eq}d_{eq}^2x}{2E_cI_cL^3}[2d_{eq}(L-x) + 2L^2 - 3Lx] & x \geq d_{eq} \end{cases}, \tag{9}$$

$$\Delta\theta = |\theta_i| + |\theta_o|, \tag{10}$$

where

$$E_cI_c = E_tI_t + E_bI_b, \tag{11}$$

$$\theta_o = \theta(x_o), \quad \text{where } x_o = \frac{L-g}{2}, \tag{12}$$

$$\theta_i = \theta(x_i), \quad \text{where } x_i = \frac{L+g}{2}, \tag{13}$$

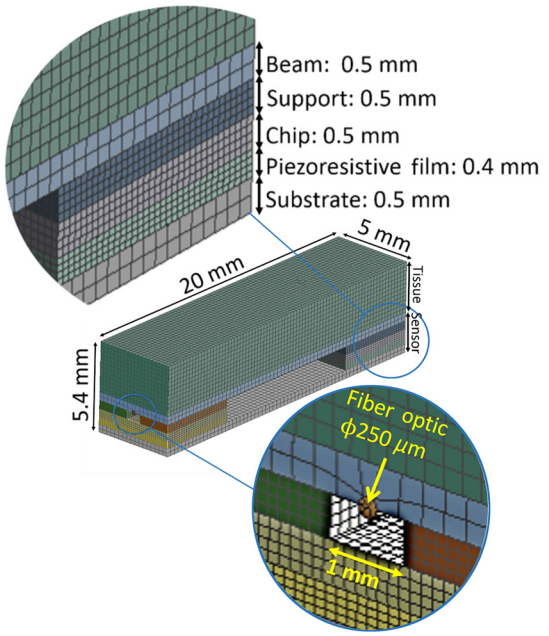

Fig. 5 Mesh quality, geometric features, and dimensions of the sensor-tissue model.

in which E_cI_c is the flexural rigidity of the composite beam, E_tI_t is the flexural rigidity of the tissue, and E_bI_b is the flexural rigidity of the beam of sensor.

Introducing the angular misalignment $\Delta\theta$, from Eq. (2), and total contact force, F_{eq}, from measurement by piezoresistive sensing elements, to Eq. (10), the unknown center of pressure, (d_{eq}) was calculated. The deflection indicated in Fig. 2 was calculated using Euler–Bernoulli beam theory. Solution of Eq. (9) for $\theta(x) = 0$ reveals the value of u_{max} [Eq. (14)]. As an angular misalignment of $\Delta\theta$ is developed in response to contact force between tissue and sensor, estimation of u_{max} is ensured in every test. Equation (15) defines the stiffness (K) as the ration of contact force (F_{eq}) to the maximum deflection of beam (u_{max}) derived from Eq. (14). The stiffness K is dependent on both the flexural rigidities of the sensor and the tissue; however, the contribution of the sensor is constant and the contribution of the tissue varies in different tissues. Therefore, as K is a function of only the stiffness of tissue, it was used for the purpose of tissue distinction.

$$u_{max} = \frac{2F_{eq}d_{eq}^3(L - d_{eq})^2}{3(E_tI_t + E_bI_b)(L + d_{eq})^2}, \tag{14}$$

$$K = \frac{F_{eq}}{u_{max}} = \frac{3(E_tI_t + E_bI_b)(L + d_{eq})^2}{2d_{eq}^3(L - d_{eq})^2}. \tag{15}$$

Depending on tissue type, d_{eq} and E_cI_c possess a specific value when the sensor touches a tissue. These values are estimated in each test using Eqs. (8)–(13). In Eq. (15), d_{eq} and E_cI_c depend only on the geometry and mechanical properties of the tissue and sensor.

3 Finite Element Modeling and Simulation

To model and predict the behavior of the sensor upon the application of an external force, or when contacting tissue, a 3-D model of the sensor was developed in CATIA V5 (6R2014, Dassault Systemes, France) and imported into ANSYS Workbench v.17 (Ansys Inc., Pennsylvania). The size and dimension of the geometric model are shown in Fig. 5. Fixed boundary conditions were applied to the sensor components. A frictionless contact condition was assumed between the sensor and the tissue phantoms.

An incompressible two-term Mooney–Rivlin (2MR) hyperelastic model was used for modeling the tissue phantoms. The 2MR hyperelastic model is well reported to successfully capture the mechanical properties of soft tissues, such as a cardiac wall, vessel wall, liver, skin, and bursae.[42] The constitutive equation of the 2MR hyperelastic material under uniaxial compression is provided in[43]

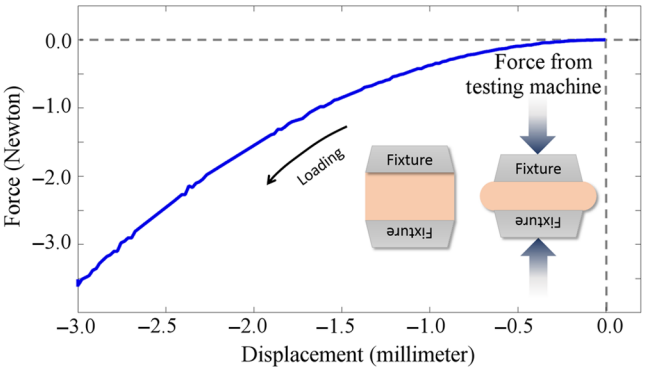

Fig. 6 Force–displacement diagram of tissue phantom material made of Ecoflex® 00-10 silicon rubber (tissue 1). The nonlinear characteristic and large deformation are evident in the force–displacement relation.

$$\sigma = 2\left(C_{10} + \frac{L_0}{L}C_{01}\right)\left[\left(\frac{L_0}{L}\right)^2 - \frac{L}{L_0}\right], \tag{16}$$

in which σ is the Cauchy axial stress, C_{01} and C_{10} are the 2MR constitutive constants, L_0 is the uncompressed length, and L is the compressed length of the material sample.

Three tissue phantom materials were synthesized using mouldable dual-component silicon rubber (Smooth On Co., Pennsylvania). Three shore hardnesses of 10-OO (extra soft), 30-OO (extra soft), and 20-A (soft) were obtained for tissues 1, 2 and 3, respectively. The constants for 2MR hyperelastic material model, C_{01} and C_{10}, were calculated for each tissue phantom as shown below.

A sample of each synthesized tissue phantom was tested during a uniaxial unconfined compression test. The mechanical tests were performed using a universal testing machine (Electroforce 3200, Bose Inc., Massachusetts). Then, the force–displacement data of each tissue phantom were used following the method reported in Ref. 31, and optimal model constants, C_{01} and C_{10}, were obtained. Figure 6 shows the nonlinear behavior of the softest tissue phantom (tissue 1) obtained during a monotonic compression test. The description, density, and mechanical properties for the constituents of the model are presented in Table 1.

The model was analyzed under two different simulations.

Table 1 Material models used in finite element modeling of the sensor-tissue simulation.

Material model	Sensor component	Material	Young's modulus (GPa)	Poisson's ratio	Density (kg/m^3)
Linear elastic	Structure	Silicon wafer	129.5	0.25	2330
	Optical fibers	—	16.5	0.4	2500
	Piezoresistor	Copper	120	0.33	8960

			Mooney–Rivlin constants		
	Tissue phantom	Material	C_{10} (kPa)	C_{01} (kPa)	Density (kg/m^3)
Hyperelastic	Tissue 1 10-OO	Ecoflex® OO-10 silicon rubber	27.147	−25.776	1040
	Tissue 2 30-OO	Ecoflex® OO-30 silicon rubber	85.157	−80.385	1070
	Tissue 3 20-A	Dragon skin® 20A silicon rubber	604.989	−573.343	1080

3.1 *Evaluation of Tissue Distinction (Simulation I)*

As shown in Fig. 7(a), the top surface of the tissue phantom, which was not in contact with the sensor, was subjected to a sinusoidal compressive force with an average amplitude of 1.3 N, at a frequency of 1 Hz. The analysis was repeated for three different tissue phantom materials. Meanwhile, the contact forces were extracted at the piezoresistive sensing elements and the relative angular misalignment between two fiber optics.

3.2 *Evaluation of Hidden Mass Detection (Simulation II)*

A spherical stainless steel inclusion, as a hidden mass, was modeled inside the tissue phantom at distance d on x-axis [Fig. 7(b)]. This method is frequently used by researchers to simulate the inclusion of a malignant tissue surrounded by normal tissue.[27,30,31,33,44–46] By this method, a sharp discontinuity in mechanical properties is incorporated to the model. Sokhanvar et al.[17] have shown that the precision of the lump detection is decreased by increasing the stiffness of tissues; therefore, the hardest material model (tissue 3) was considered as being the worst-case scenario.[17] The tissue phantom was subjected to a sinusoidal compressive displacement at its superior surface with an average of 0.5 mm at a frequency of 1 Hz. The position of the hidden mass was changed from $d = 0$ mm to $d = 20$ mm (Fig. 7). The simulation was repeated and the ration of force in the left piezoresistive sensor to the right sensor was estimated.

4 Microfabrication and Experimental Setup

The sensor was fabricated using micromachining technology. A V-groove was bulk micromachined on the bottom surface of the beam through an anisotropic wet etching process. The V-groove provided a foundation to integrate the optical fibers. Figure 8(a) shows a scanning electron microscopy (SEM) image taken from the V-groove and the integrated optical fiber in it. The smooth surface quality of the V-groove not only provided a smooth foundation on which to attach the fibers to the sensor but also led to the precise initial alignment of fibers.

Figure 8(b) shows the different structural components of the sensor before the final assembly. The silicon substrate, chips, and the supports were fabricated from an N-type ⟨100⟩ silicon wafer with a thickness of 500 μm. The substrate provides a rigid base to assemble the other components of the sensor. Two square parts of Linqstat film (piezoresistive element of required size) are sandwiched between two 200-μm thick copper electrodes [Fig. 8(c)].

The assembled sensor was calibrated following the method introduced in Ref. 31. A superluminescent diode light source (HP-371, Superlum Co., Ireland) with a central wavelength of 843 nm was connected to one fiber. The other fiber was connected to a photodetector with working wavelengths of 400 to 1100 nm (DET02AFC, Thorlabs Inc., New Jersey). The photodetector output voltage was recorded using LabVIEW software package (National Instruments Corp., Texas) and a data acquisition device (NI PCI-6225, National Instruments Corp., Texas).

The sensor and tissue phantom were assembled and secured between the fixtures of a universal testing machine (Electroforce 3200, Bose Inc., Massachusetts). The assemblies were subjected to cyclic compression testing conditions as described in simulation

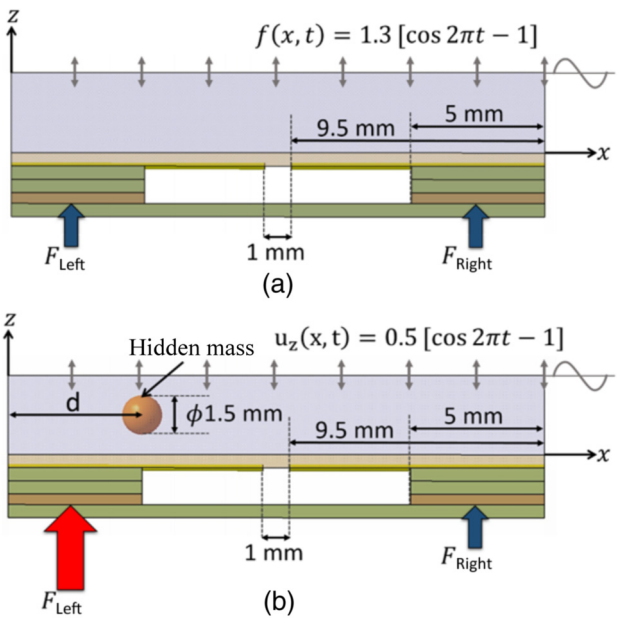

Fig. 7 (a) Schematic loading on the tissue phantom and sensor in simulation I. $f(x,t)$ is the vertical compressive force applied on the top surface of the tissue phantom and (b) the tissue phantom with a hidden mass in simulation II. $u_z(x,t)$ is the displacement boundary condition at the top surface of the tissue phantom.

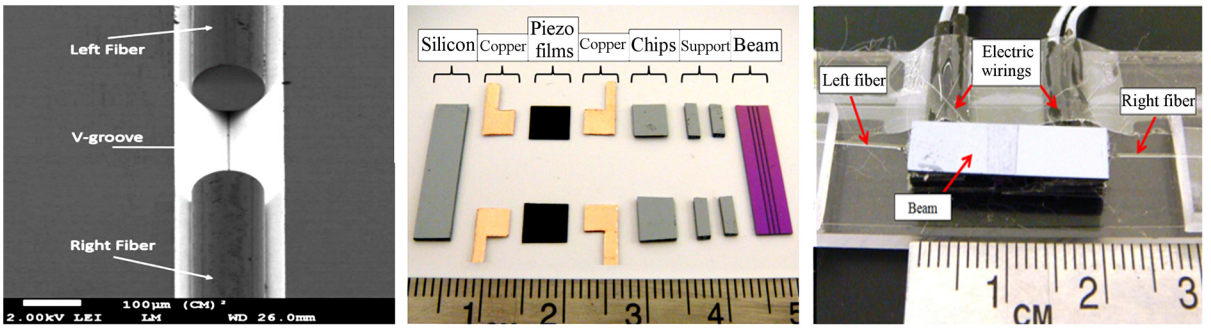

Fig. 8 (a) SEM images of the V-groove on the lower surface of the sensor beam, (b) different structural components of the sensor, and (c) final assembled sensor.

I and simulation II, while the force and displacement data were recorded. The schematic experimental system is represented in Fig. 9.

5 Results and Discussion

To evaluate the performance of the proposed sensor in estimating the stiffness of the tissue, first a harmonic finite element analysis (FEA) was performed on the model of the sensor and phantom tissue (simulation I). By obtaining the angular misalignment of two optical fibers from FEA, the change in output voltage of the photodetector was estimated following the algorithm described in Sec. 2.2. To verify the simulations, a series of experiments were performed under the same conditions as those used during the simulation procedures.

Figure 10(a) shows the estimated values of the change in output voltage of the photodetector from an FEA and the measured changes in voltage from the experiments [Fig. 10(b)] for three different tissue phantoms. The simulation results showed that

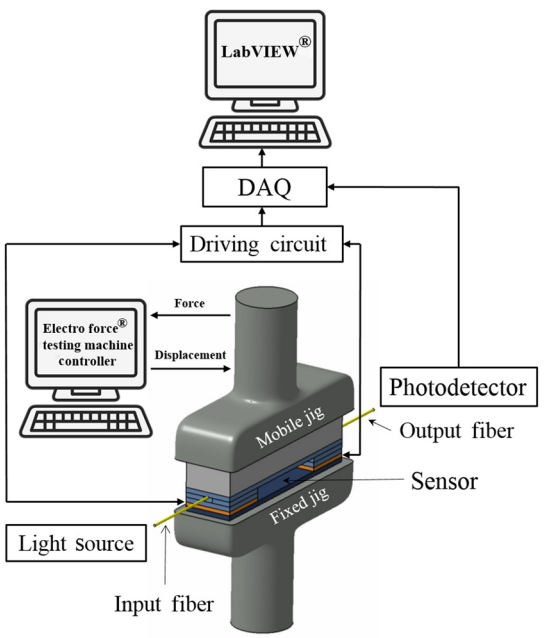

Fig. 9 Schematic experimental setup for cyclic compression. The lower jig of the testing machine was fixed and equipped with a force sensor, while the upper jig was mobile and equipped with a displacement sensor.

the maximum total force transferred to the piezoelectric sensing elements was 2.6 N, whereas the experimentally measured force was 2.47 N. It indicates a 5% error in the sensor output that could be related to the calibration coefficient of the piezoresistive elements. Other studies have reported reliable force measurements with the same order of error.[29] As the range of change in the output voltage of the photodetector (Fig. 10) is normalized with respect to its initial value, the graphs start from a unit value for both simulations and experiments.

Because the output voltage of a photodetector is a linear function of the transmitted power, it is regulated by the misalignment of two optical fibers. Considering Eqs. (2) and (5), it is inferred that smaller misalignments, due to the harder material, lead to a smaller depreciation in the output voltage. The same trend was observed in simulations and confirmed by experiments. From Fig. 10, it is evident that as the beam was being more deflected, the misalignment between the two optical fibers increased, and the transferred power decreased.

The stiffness was calculated by considering the total contact force of 2.6 N and introducing maximum deflection from Eqs. (14) to (15), for both simulations and experiments as shown in Table 2. Simulation results revealed that the smallest and largest decay in the output voltage corresponded to the hardest (tissue 3) and softest (tissue 1) phantoms, respectively. Despite a slight underestimation in the simulations, similar results for both decay in output voltage and tissue stiffness were obtained experimentally. The reason for the error could be attributed to the initial alignment of the optical fibers, erroneous physical constants, and residual errors of modeling in the material model and geometric model.

To test the capability of the sensor in finding the location of a hidden mass in the tissue phantom, the ratio of the forces in the left piezoresistive film with respect to the right piezoresistive film was used. Figure 11 shows the variation of the force ratio versus the location of the mass on the longitudinal axis of the tissue phantom. In this regard, a harmonic compressive displacement was applied on the top surface of the tissue phantom, while a stainless steel ball was inside the tissue phantom simulating a hidden mass (Fig. 7). Figure 11(a) shows the measured force at the left and right piezoresistive sensors, while the ball was located at $d = 5$ mm for tissue 3. The results revealed that the inclusion of the hidden mass in the tissue phantom led to unequal forces in the right and left piezoelectric films. This finding was in accordance with the simulation results, and the reason is due to the effect of hidden mass in shifting the center of pressure toward its location.

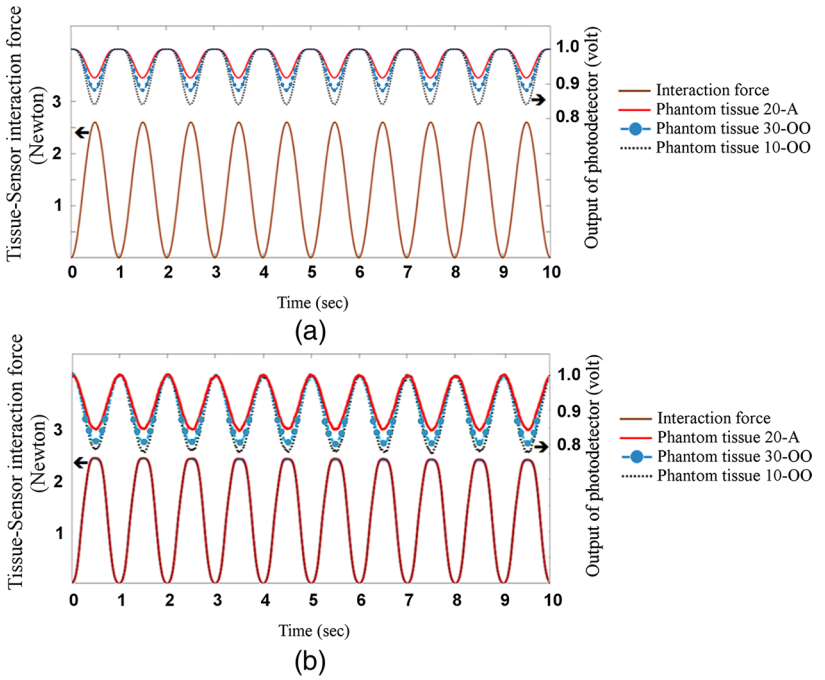

Fig. 10 Estimated force between the tissue phantoms and the sensor (left axis) and the output voltage of photodetector (right axis) resulted from the: (a) simulation I and (b) experiments.

Table 2 Normalized maximum changes in the output voltage of photodetector and stiffness from simulation and measured in the experiment.

Tissue phantom (shore hardness)	Stiffness K (N/mm)			Maximum change in output voltage (%)		
	Simulation	Experiment	Difference (%)	Simulation	Experiment	Difference (%)
Tissue 1 (10 OO)	0.24	0.31	+22.5%	16.6%	23.2%	+7.4%
Tissue 2 (30 OO)	0.73	0.84	+13.1%	11.7%	20%	+8.3%
Tissue 3 (20 A)	1.46	1.66	+12.0%	8.1%	14.4%	+6.3%

Figure 11(b) shows that as the location of the hidden mass changes toward either of the piezoresistive films, and the ratio of the forces deviates from unity. In other words, higher ratio in left to right force indicated that the mass was closer to the left film. The slope of this graph (sensitivity of the sensor to the position of hidden mass) decreases at about 75% of the length from left. The reason might be that when the mass is on the right side, due to the presence of the supports at the right side of the sensor, less change in the transmitted force to the sensor is observed. Due to the symmetry, the same phenomenon is observed for the ratio of force in the left sensor to the right (blue dashed line). This phenomenon can be calibrated by a bilinear or a nonlinear calibration rule. The same trend for the deflection in the beam in the presence of a hidden mass is reported by Ahmadi et al.[31]

According to Fig. 11(b), as the location of the hidden mass moved from left to right, the ratio of forces deviated in a range of ±3% (1.03 and 0.97). The change in this ratio from the unit is proposed as that which is used as an indicator to locate the position of a hidden mass. The results represented in Fig. 11(a) implied that the ratio of forces (left to right) was ~1.1 for $d = 5$ mm. On the other hand, the simulations predicted the ratio of forces for the same case to be slightly >1.03 (7% of error). This could prove one of the hypotheses of this study to use the ratio of forces as an indicator of the location of a hidden mass. As studied by Sokhanvar et al.,[44] the factors that could affect the transmitted force from a specific tissue phantom to a contacting sensor are the lump size, magnitude of applied load/displacement, the stiffness of the lump, and the depth of the lump in the tissue.

6 Conclusion

In this study, a hybrid optical fiber-based tactile sensor was proposed, and its capability of measuring the stiffness of the tissue was tested. In addition, the capacity of the proposed sensor in finding the location of a hidden mass was studied. In this hybrid design, the simplicity in integration, accuracy, repeatability in measurement, and linearity of response of piezoresistive sensors were used along with the biocompatibility and sensitivity of the optical fibers. In spite of the negligible discrepancy between simulated and experimental results, the response of the sensor that was subjected to dynamic loading condition was in fair agreement with the simulations and could support the main hypothesis of the hybrid design. In addition, the sensor showed high repeatability and negligible hysteresis under dynamic loading condition.

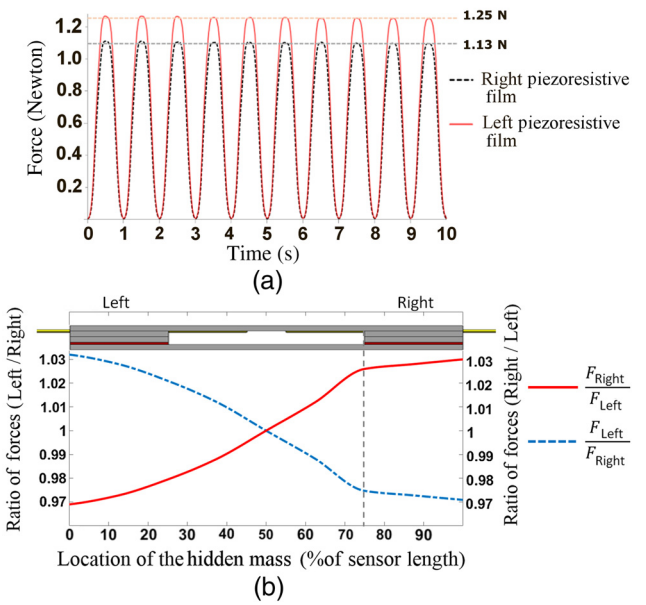

Fig. 11 (a) Variation of the force in left and right piezoresistive film with hidden mass located at $d = 5$ mm and (b) variation of the ratio of forces as a function of the location of the hidden mass.

Utilization of a sensor with the capability of *in situ* characterization of tissue is of high clinical value in robotic and MIS, where the tactile information to the surgeon is missing. Moreover, this sensor showed its capability in measuring the stiffness of an unknown tissue, which could be a uterus, vessel, nerve, lymphatic duct, etc. To investigate the clinical relevance of this sensor, one of the possible future directions could be to investigate its reliability and specificity for tissue classification. In addition, the performance of this sensor for measuring the stiffness and detecting hidden masses in heterogeneous phantom tissues is yet to be studied. In contrast to the piezoelectric sensors, the piezoresistive technology has no intrinsic limitation in measuring dynamic forces. This enables it to be utilized either in beating tissues (e.g., myocardial, vascular) or in static or quasi-static tissues (e.g., intestine, liver, prostate, kidney). Also, intrinsic scalability of the components, without compromising the sensing principles, makes the miniaturization feasible. Furthermore, the simplicity of its design (compared with array sensors) and straightforward working principle in finding the location of a hidden mass in a phantom tissue, together with its potential use in a broad field of other applications, increases its suitability for being mass produced.

Disclosures

The authors declare no conflict of financial interests.

Acknowledgments

The authors acknowledge research support from Natural Sciences and Engineering Research Council of Canada (NSERC) and Concordia University Research Chair grants of M.P. and NSERC grant of A.P.

References

1. T. L. Ghezzi and O. C. Corleta, "30 years of robotic surgery," *World J. Surg.* **40**(10), 2550–2557 (2016).
2. D. Vyas and S. Cronin, "Peer review and surgical innovation: robotic surgery and its hurdles," *Am. J. Rob. Surg.* **2**(1), 39–44 (2015).
3. B. Davies et al., "Active compliance in robotic surgery the use of force control as a dynamic constraint," *Proc. Inst. Mech. Eng. Part H* **211**(4), 285–292 (1997).
4. A. Üneri et al., "New steady-hand eye robot with micro-force sensing for vitreoretinal surgery," in *Int. Conf. on Biomedical Robotics and Biomechatronics*, pp. 814–819, IEEE (2010).
5. C. Bergeles and G.-Z. Yang, "From passive tool holders to microsurgeons: safer, smaller, smarter surgical robots," *IEEE Trans. Biomed. Eng.* **61**(5), 1565–1576 (2014).
6. C. H. King et al., "A multi-element tactile feedback system for robot-assisted minimally invasive surgery," *IEEE Trans. Haptics* **2**(1), 52–56 (2009).
7. C. H. King et al., "Tactile feedback induces reduced grasping force in robot-assisted surgery," *IEEE Trans. Haptics* **2**(2), 103–110 (2009).
8. H. Singh, R. Sedaghati, and J. Dargahi, "Experimental and finite element analysis of an endoscopic tooth-like tactile sensor," *Sensors* **1**, 259–264 (2003).
9. J. Dargahi and S. Najarian, "Theoretical and experimental analysis of a piezoelectric tactile sensor for use in endoscopic surgery," *Sensor Rev.* **24**(1), 74–83 (2004).
10. A. S. Naidu, R. V. Patel, and M. D. Naish, "Low-cost disposable tactile sensors for palpation in minimally invasive surgery," *IEEE/ASME Trans. Mechatron.* **22**(1), 127–137 (2017).
11. D. Nazarynasab et al., "A novel laparoscopic grasper with two parallel jaws capable of extracting the mechanical behaviour of soft tissues," *J. Med. Eng. Technol.* **41**, 339–345 (2017).
12. G. A. Holzapfel, "On large strain viscoelasticity: continuum formulation and finite element applications to elastomeric structures," *Int. J. Numer. Methods Eng.* **39**(22), 3903–3926 (1996).
13. Y. C. Fung, *Biomechanics: Mechanical Properties of Living Tissues*, 2nd ed., Springer, California (2013).
14. K. Chinzei, R. Kikinis, and F. A. Jolesz, "MR compatibility of mechatronic devices: design criteria," in *Int. Conf. on Medical Image Computing and Computer-Assisted Intervention*, pp. 1020–1030, Springer, Berlin (1999).
15. P. Puangmali et al., "State-of-the-art in force and tactile sensing for minimally invasive surgery," *IEEE Sensors J.* **8**(4), 371–381 (2008).
16. Y. S. Lee and K. D. Wise, "A batch-fabricated silicon capacitive pressure transducer with low temperature sensitivity," *IEEE Trans. Electron. Devices* **29**(1), 42–48 (1982).
17. S. Sokhanvar, M. Packirisamy, and J. Dargahi, "MEMS endoscopic tactile sensor: toward in-situ and in-vivo tissue softness characterization," *IEEE Sensors J.* **9**(12), 1679–1687 (2009).
18. M. H. Lee and H. R. Nicholls, "Review article tactile sensing for mechatronics—a state of the art survey," *Mechatronics* **9**(1), 1–31 (1999).
19. K. Chinzei and K. Miller, "Towards MRI guided surgical manipulator," *Med. Sci. Monit.* **7**(1), 153–163 (2001).
20. P. Polygerinos et al., "MRI-compatible fiber-optic force sensors for catheterization procedures," *IEEE Sensors J.* **10**(10), 1598–1608 (2010).
21. J. Heijmans, L. Cheng, and F. Wieringa, "Optical fiber sensors for medical applications—practical engineering considerations," in *4th European Conf. of the Int. Federation for Medical and Biological Engineering*, pp. 2330–2334, Springer, Berlin (2009).
22. I. Gannot, *Optical Fibers and Sensors for Medical Applications*, Vol. **4616**, p. 237, SPIE Press, Bellingham, Washington (2002).
23. M. C. Yip, S. G. Yuen, and R. D. Howe, "A robust uniaxial force sensor for minimally invasive surgery," *IEEE Trans. Biomed. Eng.* **57**(5), 1008–1011 (2010).
24. S. Elayaperumal et al., "Detection of membrane puncture with haptic feedback using a tip-force sensing needle," in *Int. Conf. Intelligent Robots and Systems*, pp. 3975–3981, IEEE (2014).
25. Y. Qiu et al., "Quantitative optical coherence elastography based on fiber-optic probe with integrated Febry–Perot force sensor," *Proc. SPIE* **9702**, 97020W (2016).
26. Y. Noh et al., "Image-based optical miniaturized three-axis force sensor for cardiac catheterization," *IEEE Sensors J.* **16**(22), 7924–7932 (2016).
27. R. Ahmadi et al., "Discretely loaded beam-type optical fiber tactile sensor for tissue manipulation and palpation in minimally invasive robotic surgery," *IEEE Sens. J.* **12**(1), 22–32 (2012).

28. R. Ahmadi, M. Packirisamy, and J. Dargahi, "Innovative optical microsystem for static and dynamic tissue diagnosis in minimally invasive surgical operations," *J. Biomed. Opt.* **17**(8), 081416 (2012).
29. R. Ahmadi, M. Packirisamy, and J. Dargahi, "High sensitive force sensing based on the optical fiber coupling loss," *J. Med. Devices* **7**(1), 011001 (2013).
30. R. Ahmadi et al., "Micro-optical force distribution sensing suitable for lump/artery detection," *Biomed. Microdevices* **17**(1), 10 (2015).
31. R. Ahmadi et al., "A multi-purpose optical microsystem for static and dynamic tactile sensing," *Sens. Actuators, B* **235**, 37–47 (2015).
32. Kalantari et al., "A piezoresistive tactile sensor for tissue characterization during catheter-based cardiac surgery," *Int. J. Med. Rob. Comput. Assisted Surg.* **7**(4), 431–440 (2011).
33. S. Sokhanvar et al., "Graphical rendering of localized lumps for MIS applications," *J. Med. Device* **1**(3), 217–224 (2007).
34. S. Phipps, "Measurement of tissue mechanical characteristics to distinguish between benign and malignant prostatic disease," *Urology* **66**(2), 447–450 (2005).
35. T. A. Krouskop, "Elastic moduli of breast and prostate tissues under compression," *Ultrason. Imaging* **20**(4), 260–274 (1998).
36. C. Walter et al., "Increased tissue stiffness in tumors from mice with neurofibromatosis-1 optic glioma," *Biophys. J.* **112**(8), 1535–1538 (2017).
37. S. Nemoto and T. Makimoto, "Analysis of splice loss in single-mode fibres using a Gaussian field approximation," *Opt. Quantum Electron.* **11**(5), 447–457 (1979).
38. J. Li, Q. Zhang, and A. Liu, "Advanced fiber optical switches using deep RIE (DRIE) fabrication," *Sens. Actuators B Phys.* **102**(3), 286–295 (2003).
39. P. Puangmali, K. Althoefer, and L. D. Seneviratne, "Mathematical modeling of intensity-modulated bent-tip optical fiber displacement sensors," *IEEE Trans. Instrum. Meas.* **59**(2), 283–291 (2010).
40. G. P. Agrawal, *Nonlinear Fiber Optics*, 4th ed., Academic Press, Florida (2007).
41. F. Beer et al., *Mechanics of Materials*, 7th ed., McGraw-Hill, New York (2015).
42. F. Peyraut et al., "Modeling of biological tissues with anisotropic hyperelastic laws—Theoretical study and finite element analysis," *C. R. Mecanique* **337**(2), 101–106 (2009).
43. R. Rivlin, "Large elastic deformations of isotropic materials. IV. Further developments of the general theory," *Philos. Trans. R. Soc. A* **241**(835), 379–397 (1948).
44. S. Sokhanvar, J. Dargahi, and M. Packirisamy, "Hyperelastic modelling and parametric study of soft tissue embedded lump for MIS applications," *Int. J. Med. Rob. Comput. Assisted Surg.* **4**(3), 232–241 (2008).
45. X. Jia et al., "Lump detection with a gelsight sensor," in *World Haptics Conf.*, pp. 175–179, IEEE, Daejeon (2013).
46. J. C. Gwilliam, "Human vs. robotic tactile sensing: detecting lumps in soft tissue," in *Haptics Symp.*, pp. 21–28, IEEE, Massachusetts (2010).

Naghmeh M. Bandari received her bachelor's and master's degrees in biomedical engineering from Amirkabir University of Technology, Iran. She was with Medtronic Inc.'s agent in Iran for four years, as the supervisor in CoreValve® therapy development team. Currently, she is a PhD candidate at Optical-Bio MEMS, and Tactile Sensing and Medical Robotics Laboratory, Department of Mechanical and Industrial Engineering, Concordia University, Canada. Her research focus is on development of optical tactile sensors with application in minimally invasive surgery.

Roozbeh Ahmadi received his BSc degree in mechanical engineering from Tabriz University, Iran, his MSc degree in mechatronics engineering from the Iran University of Science and Technology (IUST) and his PhD from Concordia University. He worked towards his PhD at Optical-Bio-Microsystems Laboratory and at Tactile Sensing and Medical Robotics Laboratory, Department of Mechanical and Industrial Engineering, Concordia University, Canada. His research interests include optical-fiber-based sensors, haptic/tactile devices, minimally invasive surgery, medical robots, and MEMS.

Amir Hooshiar received bachelor's and master's degrees in biomedical engineering with honors from Amirkabir University of Tehran, Iran. He focused on mechanical testing and modeling of bone tissue in his masters and served as a certified medical devices expert for nine years. He is a winner of FRQNT scholarship, an NSERC Vanier scholar and PhD candidate in Robotic Surgery Laboratory at Concordia University, Canada. His research is on the application of nonlinear structural mechanics in robotic cardiac interventions.

Javad Dargahi is a professor in the Department of Mechanical and Industrial Engineering, Concordia University, Canada. He is the coauthor of a book, *Artificial Tactile Sensing in Biomedical Engineering* (McGraw-Hill). He also has a patent titled "System for sensing and displaying force and softness." He has published 140 refereed journal and conference papers. His research area includes design and fabrication of haptic sensors and feedback systems for minimally invasive surgery and robotics, micromachined sensors and actuators.

Muthukumaran Packirisamy is a professor and Concordia research chair at Concordia University, Canada. He is the recipient of Member Royal Society of Canada College, fellow of CAE, CSME, ASME and IE(I), and I. W. Smith Award from CSME, Concordia University Research Fellow, Petro Canada Young Innovator Award, and ENCS Young Research Achievement Award. As an author of more than 400 articles published in journals and conferences and 15 inventions, he supervised more than nine research associates and 66 graduate students.